applied sciences

MDPI

Article

Effect of Radial Leakage on Combustion Characteristics in Rotary Engines: Experimental and Numerical Investigation

Yi Zhang [1], Liangyu Li [2,*], Yanzhe Liu [2], Shiliang Yao [1] and Run Zou [1]

[1] School of Energy and Power Engineering, North University of China, Taiyuan 030051, China; zhangyi@nuc.edu.cn (Y.Z.); zourun@nuc.edu.cn (R.Z.)
[2] School of Mechanical and Electrical Engineering, North University of China, Taiyuan 030051, China
* Correspondence: 20250117@nuc.edu.cn

Abstract

To further investigate the influence of the law of leakage on rotary engines, this study took a single-cylinder gasoline rotary engine as the research object and analyzed the effects of radial leakage, using the experimentally validated 3D combustion simulation model as the basis, and equivalent leakage area on in-cylinder flow, combustion process, and engine performance. The study shows the following: on the one hand, leakage disperses the force exerted by the rotor on the in-cylinder fluid and flame, thereby changing the fluid direction; on the other hand, it increases the distribution area of high-speed fluid in the middle and rear parts of the combustion chamber and reduces the overall flow velocity in the front part. Radial leakage has the characteristics of both a slight positive promotion and a negative interference on combustion, and the increase in equivalent leakage area will strengthen the negative effect. Meanwhile, it reduces the combustion efficiency, causes a significant decrease in cylinder pressure and maximum cylinder temperature, and exerts an adverse impact on the overall performance of the engine.

Keywords: rotary engines; radial leakage; systematic study on influence laws

check for updates

Received: 10 October 2025
Revised: 10 November 2025
Accepted: 17 November 2025
Published: 21 November 2025

Citation: Zhang, Y.; Li, L.; Liu, Y.; Yao, S.; Zou, R. Effect of Radial Leakage on Combustion Characteristics in Rotary Engines: Experimental and Numerical Investigation. *Appl. Sci.* **2025**, *15*, 12371. https://doi.org/10.3390/app152312371

1. Introduction

Rotary engines, renowned for their advantages such as high power density, low vibration, and stable output [1], are widely used in fields including aerospace and the automotive industries [2]; however, they also have some issues [3]—under high-load and high-speed conditions, rotary engines are prone to leakage, which significantly affects the combustion process, thermal efficiency, and emission performance [4], and their leakage modes mainly consist of radial and end-face leakage, which not only leads to incomplete combustion and power loss but also may cause combustion instability, increase emissions [5], and affect the reliability and service life of the engine. Although some studies have explored the impact of leakage on engine performance, research on the influence law of radial leakage on the combustion process in rotary engines remains relatively insufficient.

In recent years, numerous scholars have conducted research on the impact of leakage on engine performance in rotary engines. Chen et al. [6] adopted an experimental method to investigate the influence of geometric and aerodynamic parameters on cold air leakage through pressure and mass flow measurement, and the results showed that the proportions of bypass leakage and clearance leakage in total leakage change with the variation in plate spacing, and, when the shroud clearance is fixed, the proportion of clearance leakage in total leakage gradually increases. Kim et al. [7] analyzed the results of three leakage paths, i.e., from the compressor outlet to the cold-side outlet of the heat exchanger, from the compressor outlet to the combustor outlet, and from the combustor inlet to the turbine outlet, and found that the third path caused the most significant reduction in engine efficiency. Ai et al. [8] designed an experimental system to study the influence of loading parameters and structural parameters on the sealing performance of aero-engine casing flanges, and the results indicated that increasing the surface roughness from 1.6 to 3.2 would lead to an increase in leakage volume by 26 L/min. Turnbull et al. [9] studied the effects of transient ring elastodynamics and hot gas flow through piston gaps on chamber leakage pressure and parasitic friction loss, and the results showed that the power loss caused by gas leakage may be six times greater than that caused by friction loss. Jiaqiang et al. [10] developed an improved thermodynamic model for thermodynamic parameters to study cold-start capability, and it was found that, when the adiabatic index of the compressed gas is 1.34, the prediction of ignition temperature is closest to the experimental value, while the thermodynamic results revealed that the compression pressure is the most sensitive to the gas leakage rate, followed by the heat transfer loss rate and reference clearance volume. Hu et al. [11] proposed a new fault diagnosis method for diesel engine valve leakage, which can be transferred from one working condition or type to another to enhance the generalization of fault diagnosis. Fan et al. [12] developed and validated a 3D dynamic simulation model considering apex seal leakage through 2D PIV experiments, numerically investigated the flow field formation mechanisms of the rotary engine with compound intake ports under different apex seal leakage gaps (0.02, 0.04, 0.06, and 0.08 mm) and engine speeds (2000, 3500, and 5000 rpm), and found that there are two formation mechanisms of the flow field in the intake stroke, namely, "side intake port dominance" and "peripheral intake port dominance", and, under the selected speeds, the flow field mechanism gradually shifts from the former to the latter as the leakage gap increases. Yang et al. [13] proposed and compared two methods for calculating the leakage area of the spark plug cavity, among which the method based on leakage direction is more consistent with the experimental results, and his research found that the leading spark plug leakage and corner seal leakage have the most significant impacts on peak pressure and IMEP (Indicated Mean Effective Pressure), reducing the peak pressure by 0.249 MPa and 0.047 MPa, respectively, decreasing the IMEP by 8.68% and 10.51%, respectively. In addition to reducing the leakage area, reducing the distance between the front spark plug and the minor axis by 5.5 mm can increase the peak pressure by 0.2 MPa and reduce the leakage from the working chamber to the adjacent chamber from 0.055 g to 0.038 g. Fan et al. [14] established a 3D dynamic simulation model considering apex seal leakage and verified this model through Particle Image Velocimetry (PIV) results and in-cylinder pressure experimental results. Picard et al. [15] proposed a modeling method to evaluate the gas leakage of apex seals and corner seals in rotary engines, and the study showed that the leakage through the contact surface between the seal and the housing is negligible, because the apex seal can adapt to the deformed shape of the rotor housing.

Other scholars, on the other hand, have focused their research on the impact of engine leakage on combustion and overall engine performance, leakage-related diagnosis methods, and combustion-adapted control strategies. Zhou et al. [16] realized the system-level prediction of clearance leakage in micro rotary engines by solving the Navier–Stokes equations. Fan et al. [17] established a 3D dynamic calculation model of rotary engines considering apex seal leakage, and studied the influence of apex seal leakage on the velocity field, turbulent kinetic energy, and volumetric efficiency in the combustion chamber. Ji et al. [18] established a pressure prediction and apex seal vibration model to analyze the mechanisms of GLA (Gas Leakage Amount) and DLA (Dynamic Leakage Amount), as well as the influence of key parameters on them. The results showed that DLA decreases with the increase in the discharge coefficient and the clearance between the apex seal and the groove, and there is no DLA when the rotational speed is lower than 2000 rpm or higher than 7000 rpm. Fan et al. [19] established a 3D model considering apex seal leakage to study the combustion process of natural gas/hydrogen rotary engines under various HIA (Hydrogen Injection Amount) and HIT (Hydrogen Injection Timing) conditions, and proposed the ideal hydrogen distribution for ignition timing that can improve combustion efficiency. Fan et al. [20] studied the influence of different injection strategies on the combustion process of rotary engines under the premise of radial seal leakage of the rotor. Shi et al. [21] pointed out that one of the effective methods to solve the incomplete combustion problem of rotary engines is direct injection technology. Ji et al. [22] improved ignition and combustion by adopting a passive pre-chamber, and the results indicated that low temperature tends to inhibit flame propagation, while TJI (Turbocharged Jet Ignition) can accelerate flame speed and promote flame propagation to the unburned area of the combustion chamber, and combining low-temperature hydrogen with a passive pre-chamber can achieve high thermal efficiency and power of the engine while significantly reducing leakage. Yang et al. [23] obtained the conclusion through repeated experiments on the moving distance of the leading spark plug and measuring the in-cylinder peak pressure, indicated thermal efficiency, and the mass of leaked fresh mixture that the indicated thermal efficiency reaches the maximum when the moving distance of the leading spark plug is -6.5 mm, while the peak pressure and indicated thermal efficiency will decrease when the moving distance of the leading spark plug exceeds -6.5 mm, and the residual gas with excessive leakage has a negative impact on combustion.

In summary, systematic research on the leakage characteristics of radial leakage and equivalent leakage area in rotary engines is relatively scarce at the current stage. This work can provide design schemes and theoretical support for its applications in the transportation, marine, and aerospace fields [24]. Thus, based on the experimentally validated 3D combustion simulation model of rotary engines, this paper establishes a leakage model of rotary engines that includes radial leakage, deepens the research from the impact of radial leakage on the macro-performance of rotary engines to its impact on the micro-combustion process of rotary engines, analyzes the influence laws and mechanism of the equivalent leakage area on the in-cylinder gas flow and combustion process of the engine under the effect of radial leakage, supplements the theoretical basis and influence laws of the impact of radial leakage on rotary engines, provides a basis for the quantitative evaluation of the leakage characteristics of rotary engines, and will play a key role in achieving the carbon neutrality goal [25].

2. Establishment and Validation of a 3D Simulation Model for Rotary Engines

The in-cylinder working process of a rotary engine includes intake, compression, power, and exhaust strokes. The engine cylinder block is an important component of engines and various power vehicles, featuring complex working conditions and high requirements, and is usually an integral casting [26]. In-cylinder fluid flow, including one-way flow and vortex flow, belongs to complex turbulent flow, and, especially during the power stroke, it is a complex turbulent combustion process involving chemical reactions. Therefore, establishing an appropriate 3D combustion simulation model for rotary engines requires selecting reasonable turbulence models, combustion models, ignition models, and fuel reaction mechanisms, which can improve the system performance and stability in its application [27]. To accurately simulate the in-cylinder flow and combustion process of rotary engines, the computational models and chemical reaction mechanisms selected in this study are shown in Table 1. The RNG $k-\varepsilon$ (Renormalization $k-\varepsilon$ Group

Model) can take into account the streamline curvature, vortexes, and mechanical changes in the rotary engine cylinder [28], making the computational results more accurate. The SAGE (Software for the Analysis of Gas phase chemistry and Aerosol formation in the Environment) combustion model can obtain the component distribution and concentration variation process during the combustion process of rotary engines, thereby accurately simulating the combustion process. Regarding the ignition model, this study adopts spark plug ignition, and the ignition model uses a virtual spherical spark with a diameter of 1 mm and an ignition energy of 0.08 J to replace the actual spark plug kernel for triggering the combustion reaction of the mixture in the combustion chamber.

Table 1. Mathematical models and chemical reaction mechanisms.

Model Type	Model Selection and Mechanism
Turbulence Model	RNG $k-\varepsilon$ Model
Combustion Model	SAGE Model
Ignition Model	Spark-Energy Deposition Model
Reaction Mechanism	Skeletal Mechanism

This study takes a single-cylinder gasoline rotary engine as the research and validation object, and Table 2 presents the structural parameters of this rotary engine; the solid model established based on the above parameters is shown in Figure 1.

Table 2. Structural parameters of the rotary engine.

Parameter Name	Value
Generating Radius (mm)	60
Eccentricity (mm)	10
Cylinder Block Thickness (mm)	41.2
Rated Speed (r/min)	8000
Single-Cylinder Displacement (cc)	133
Compression Ratio	10
Ignition Advance Angle	30 °CA BTDC (Before Top Dead Center)
Ignition Source	Single Spark Plug

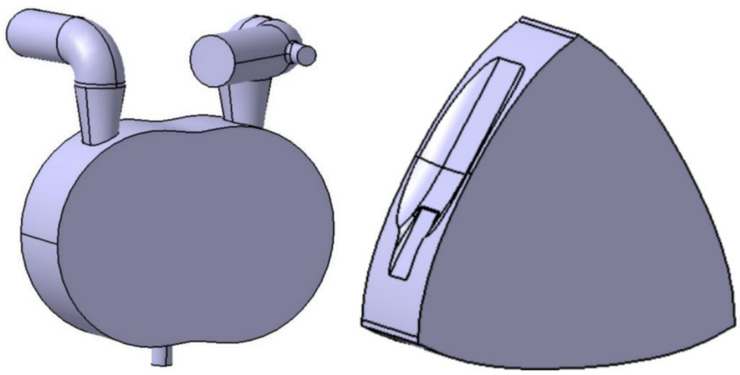

(**a**) (**b**)

Figure 1. Three-dimensional model. (**a**) Cylinder fluid domain, (**b**) rotor solid.

This study divides the three-segment recess of the rotary engine into four parts—front part of the recess, middle part of the recess, rear part of the recess, and spoiler—using the rotation direction as the identifier, the structural schematic diagram of which is shown in Figure 2, with the rotation direction of the rotor in the following text being clockwise and the origin of the 3D coordinate system located at the center of gravity of the rotor.

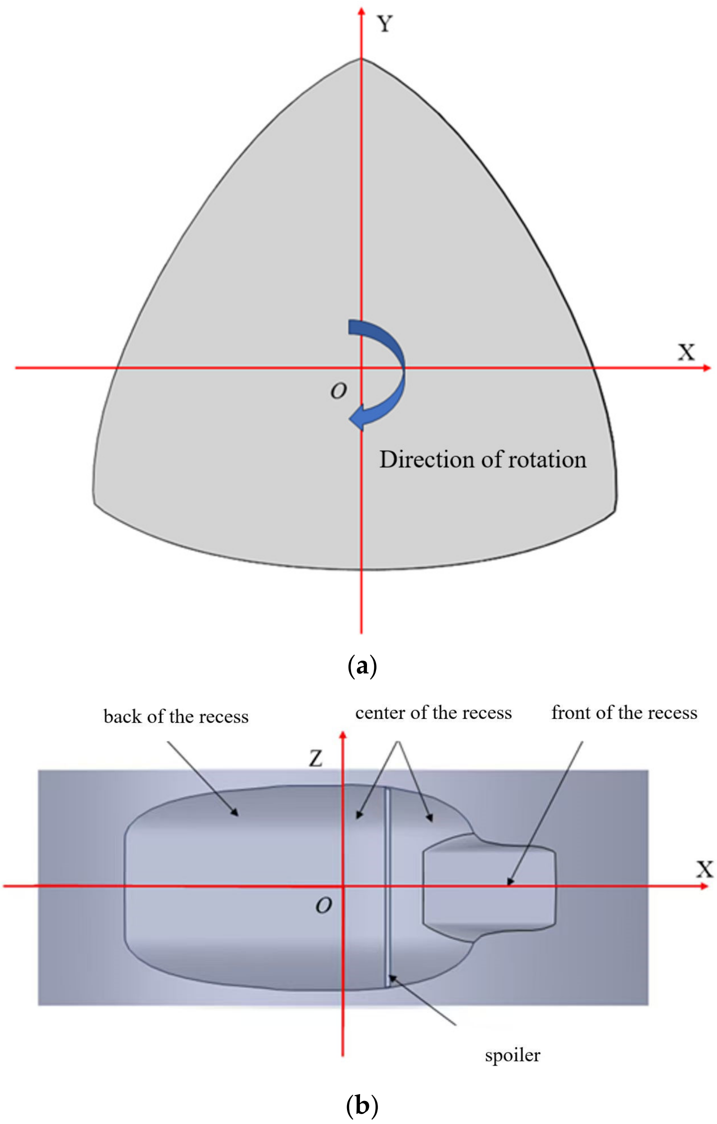

Figure 2. Schematic diagram of the rotor structure. (**a**) Front view of the XY plane, (**b**) bottom view of the XZ plane.

Since the number of meshes has a certain impact on the calculation results, it is necessary to conduct mesh independence analysis on the simulation model before performing actual simulation calculations—to eliminate the influence of the mesh number on the calculation results, ensure calculation accuracy, and select the most appropriate mesh number to reduce calculation time. In this study, with the boundary conditions kept unchanged, the in-cylinder pressure changes under four different mesh numbers were compared; the boundary conditions of the rotary engine were set as shown in Table 3.

Table 3. Boundary conditions of the rotary engine.

Boundary Region	Temperature (K)	Pressure (MPa)
Intake Port	300	0.101325
Intake Manifold	300	/
Exhaust Port	570	0.101325
Exhaust Manifold	550	/
Rotor	400	/
Spark Plug	624	0.117210
Spark Electrode	600	/

Figure 3 shows the pressure change curves under different mesh numbers. Based on a 2 mm mesh, Adaptive Mesh Refinement (AMR) was adopted, and the cylinder pressure change curve was basically consistent with that of the 1 mm mesh, with the calculation results tending to be stable.

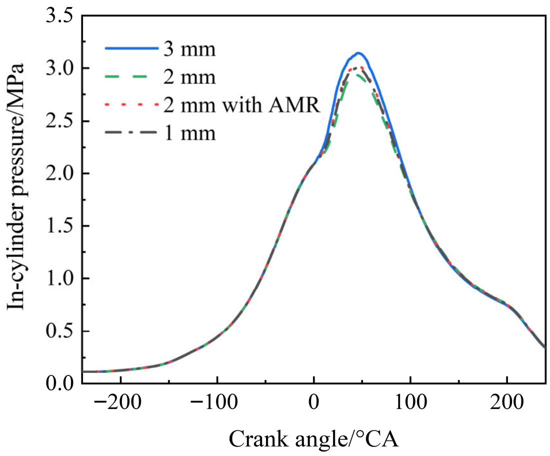

Figure 3. In-cylinder pressure variation curves under different mesh numbers.

This study uses CONVERGE 3.0 software to simulate the in-cylinder combustion process of the rotary engine, which is equipped with Adaptive Mesh Refinement (AMR) technology and can dynamically refine the mesh in the fluid domain based on changes in temperature and velocity, thereby improving solution efficiency and accuracy. In this study, a three-level Adaptive Mesh Refinement based on temperature and velocity is set for the entire fluid domain, and, due to the high temperature and velocity at the end of the compression stroke, the mesh around the spark plug is further refined to improve calculation accuracy, while the mesh in other regions of the cylinder maintains the base size. The base mesh scheme used in this study is 2 mm, and, during the combustion process, the fluid domain is set with Adaptive Mesh Refinement and two-level fixed refinement, so the actual mesh size is 0.58 mm. For typical engine simulations using the RANSs (Reynolds-averaged Navier–Stoke) model, the minimum length scale is approximately 0.1 to 1 mm, and, when a fine mesh size of 0.58 mm is used, sharp gradients in temperature and density are unlikely to exist. Combined with the relevant literature [29–31], the model established in this study has sufficient mesh resolution in RANS simulations and can use detailed chemical models to obtain accurate combustion results. Their distribution is shown in Figure 4.

To ensure the calculation accuracy of the 3D CFD (Computational Fluid Dynamics) simulation model for the rotary engine established in this study, an experimental test bench is established to validate the combustion model at the rated speed. The fuel used in the rotary engine is Sinopec National V 92# (Sinopec Group Corporation, Beijing, China) commercial gasoline, and, to meet the lubrication requirements of the rotary engine for structures such as in-cylinder rotors and sealing plates, Motul-710 (Motul China, Shanghai, China) ester-based fully synthetic engine oil is mixed into the fuel at a 1:50 volume mixing ratio [32].

The ignition system and fuel supply system of the rotary engine studied in this paper are controlled by an electronic ignition module and an electronic fuel injector, respectively. The electronic ignition module is composed of a power supply, sensors, an electronic control unit, an ignition controller, an ignition coil, a distributor, and other components, with its ignition energy provided by an external power supply. Compared with other ignition systems, electronic ignition has advantages, such as good ignition angle control accuracy, a wide adjustment range of ignition strategies, a simple structure of the ignition module, and good ignition performance at low speeds [33]. The electronic fuel injector is composed of a solenoid valve assembly, a needle valve assembly, and a nozzle assembly, and, compared with traditional mechanical fuel injectors, it can dynamically adjust injection strategies, including fuel injection timing and injection pulse width, according to changes in operating conditions. In order to comprehensively control the engine operating conditions, the experimental test bench uses an electronic control unit to comprehensively regulate the fuel injection strategy and ignition strategy. Figure 5 shows the electronic ignition module, electronic fuel injector, and electronic control unit of the rotary engine.

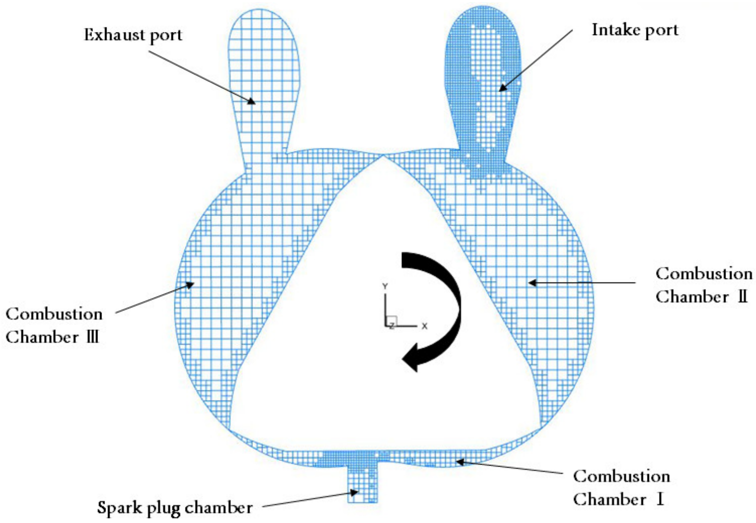

Figure 4. Computational mesh of rotary engines.

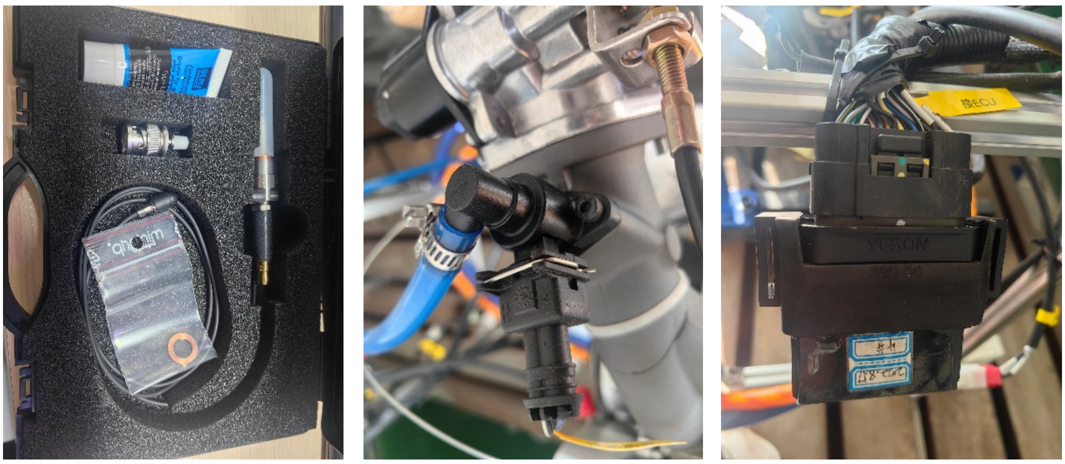

(**a**) (**b**) (**c**)

Figure 5. Control modules of the rotary engine. (**a**) Electronic ignition module, (**b**) electronic fuel injector, (**c**) electronic control unit.

Figure 6 shows the schematic diagram of the experimental test bench structure for the rotary engine established in this study, in which the rotary engine is connected to an SSCG45 electric dynamometer produced by Xunlan Intelligent Technology Co., Ltd. (Shenzhen, China)—this dynamometer is used to control and detect the rotary engine's speed, power, and torque (rated power: 45 kW; maximum speed: 10,000 r/min; range: ±100 N·m; accuracy: 0.2% FS). A Model 6113CF-3AQ01-4-1 spark plug-type pressure sensor produced by Kistler (Winterthur, Switzerland) is used to measure the average in-cylinder pressure of the rotary engine (maximum measurement error of in-cylinder pressure: ±0.05 MPa). A photoelectric crankshaft position sensor is used to collect crankshaft position signals, and the in-cylinder pressure sensor signals and crankshaft position signals are transmitted to the combustion analyzer via shielded cables. An oxygen sensor is used to measure the excess air ratio at the exhaust pipe, which is then transmitted to the A/F (Air/Fuel) ratio analyzer. All the above data are aggregated into a Model TCM-1000 comprehensive measurement and control system for the rotary engine test bench produced by Siemens (Munich, Germany), and this system sends control information, including ignition strategies and fuel injection strategies, to the rotary engine.

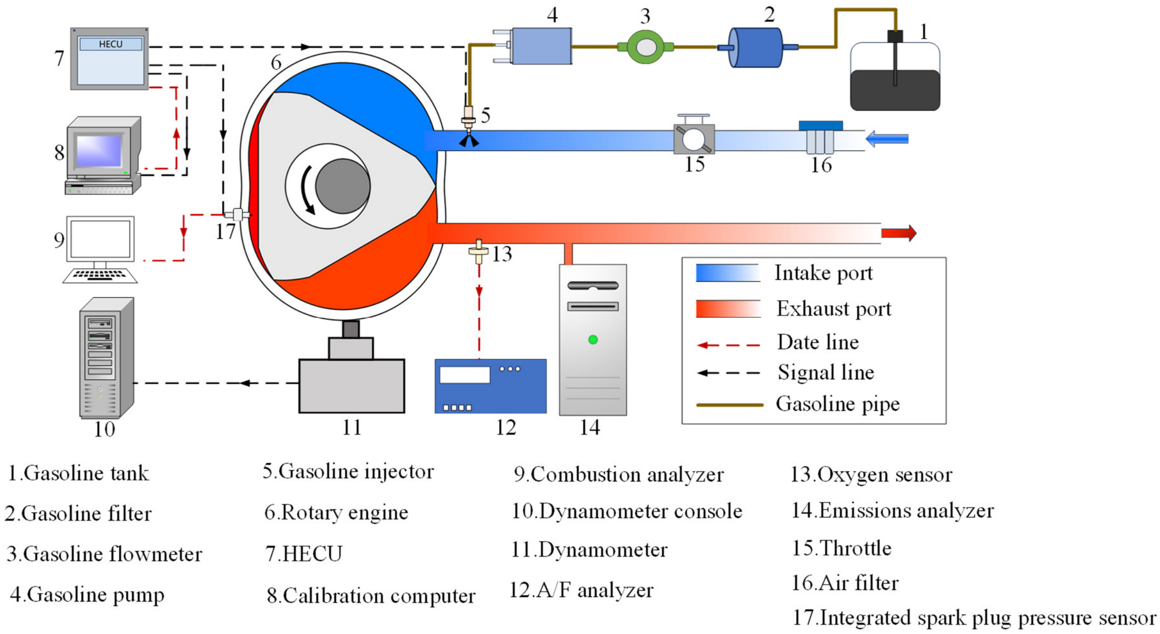

Figure 6. Structural schematic diagram of the rotary engine experimental test bench.

Figure 7 shows the rotary engine experimental test bench and Figure 8 shows the comprehensive measurement and control system of the rotary engine experimental test bench. This experimental test bench is based on a certain type of peripheral-intake single-spark-plug intake port premixed gasoline triangular rotor engine [34]. It has completed the design, assembly, and debugging of the software and hardware of the rotary engine's electronic control system, and has achieved high-precision control of fuel injection strategies and ignition strategies [35], as well as having completed the collection of in-cylinder pressure of the rotary engine under rated operating conditions, providing boundary conditions and verification data for the establishment and validation of the 3D combustion simulation model of the rotary engine.

To ensure the calculation accuracy of the 3D CFD (Computational Fluid Dynamics) simulation model for the rotary engine established in this study, the combustion model under the original combustion chamber structure and original ignition scheme was validated. Under the operating conditions of ignition timing at −30 °CA, intake pressure at 101,325.0 Pa, rotational speed at 8000 r/min, and gasoline as fuel, the comparison between the simulation results and experimental results of in-cylinder pressure is shown in Figures 9 and 10. The experimental in-cylinder pressure curve in Figure 9 is data obtained by averaging over multiple cycles after data cleaning and filtering (i.e., removing obvious outliers and filtering the signal to reduce noise interference), while the simulated in-cylinder pressure curve is data from a single cycle after the combustion of the 3D combustion simulation model of the rotary engine stabilizes. Figure 10 shows the relative error values obtained by extracting data (or performing interpolation calculations) from the simulation results at positions exactly corresponding to the experimental measurement points, after time alignment and with the experimental in-cylinder pressure as the error base. It can be seen from the figures that the simulation results are in good overall agreement with the experimental results, with errors less than 5% in the range of −50 °CA to 100 °CA. Thus, it is indicated that the 3D combustion model constructed in this study can accurately predict the combustion process of the rotary engine, with high reliability of its simulation data, and can be used for subsequent related research and analysis.

Figure 7. Rotary engine experimental test bench.

Figure 8. Comprehensive measurement and control system of the rotary engine experimental test bench.

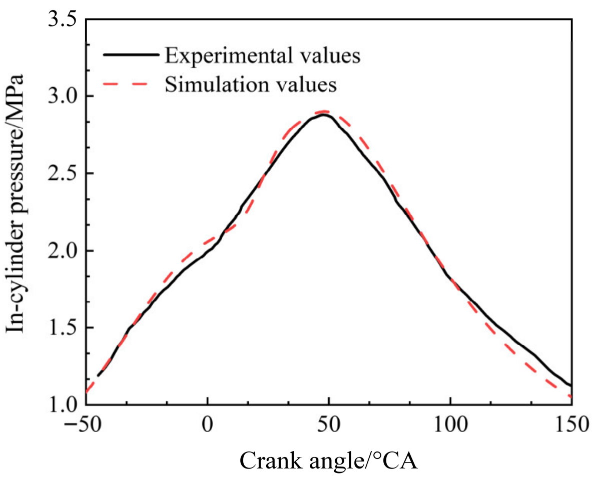

Figure 9. Comparison of In-Cylinder Pressure.

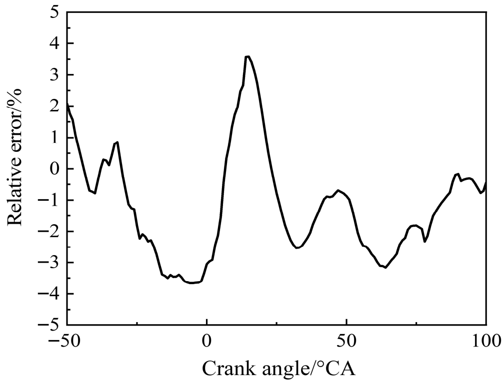

Figure 10. Comparison of relative errors.

3. Theoretical Analysis of Radial Leakage and Establishment of the Simulation Model

The radial sealing elements of the rotary engine are installed at the rotor tips [36]. Affected by centrifugal force, these sealing elements move in the sealing grooves, and their structural schematic diagram is shown in Figure 11. Radial sealing consists of two parts: the primary seal and the secondary seal. The primary seal, as the main component responsible for radial leakage, is mainly composed of one radial primary sealing element and one radial triangular sealing element [37], and is loaded by leaf springs to ensure continuous contact between the sealing elements and the sealing surface [38]. The positions where the two ends of the primary seal come into contact with the axial sealing elements are affected by rotor movement and serve as the weak links of radial sealing, and so two radial apex sealing elements are installed to adapt to the relative movement between the rotor and the axial sealing elements. Each radial apex sealing element is independently loaded by a cylindrical spring to maintain continuous contact between the sealing elements and the sealing surface [39,40].

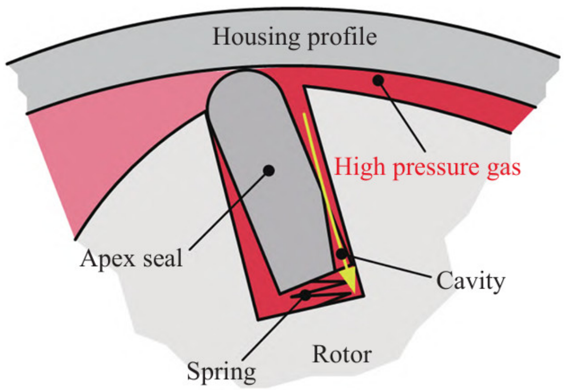

Figure 11. Radial sealing schematic diagram.

There are three possible leakage paths in the radial seal, namely, geometric leakage, leakage between the rotor and the sealing plates, and leakage between the sealing plate grooves and the sealing plates. Geometric leakage refers to the gaps between the radial seal components, which are caused by thermal deformation, mechanical deformation, and manufacturing tolerances of the components. Leakage occurs between the rotor and the running surface of the sealing elements when the force on the apex is unbalanced and the sealing elements separate from the rotor [41]. Leakage occurs between the sealing plate grooves and the sealing plates when the radial seal moves from one side of the sealing plate groove to the other under the action of pressure changes [42].

3.1. Theoretical Analysis of Radial Leakage Forms

In the operating state, the calculation of the clearance of the sealing plates relative to the cylinder block is shown in Equation (1):

$$h_c(x_c) = D + \frac{x_c^2}{2a_a} - y_g cos\,\varnothing_a + x_g sin\,\varnothing_a + \alpha_g\left(x_c - H_p sin\,\varnothing_a\right) \quad (1)$$

In the equation, x_c denotes the position along the rotation direction of the cylinder block, D denotes the theoretical distance between the cylinder block and the seal plate, a_a denotes the radius of the arc at the top of the seal plate, φ_a denotes the distance between the top of the seal plate and the cylinder block, x_g and y_g denote the lateral and radial displacements of the seal plate, respectively, a_g denotes the tilt angle of the seal plate, and H_p denotes the distance between the center of mass of the seal plate and the center of the arc at the top of the seal plate.

The calculation of the clearance of the sealing plates in the sealing grooves is shown in Equation (2):

$$h_b(y_b) = \frac{\Delta G}{2} + x_g - (y_b - H_l)\alpha_g + h_{wb} + h_{eb} \quad (2)$$

In the equation, x_c denotes the position on the seal plate groove, G denotes the theoretical clearance between the seal plate groove and the seal plate, a_a denotes the distance from the bottom of the seal plate to its center of mass, h_{wb} denotes the wear of the seal plate, h_{eb} denotes the wear of the seal plate groove, a_g denotes the tilt angle of the seal plate, and H_p denotes the distance between the center of mass of the seal plate and the center of the arc at the top of the seal plate.

In Equations (1) and (2), both D and ΔG must be obtained through thermomechanical load calculation.

The calculation of the roughness contact pressure of the sealing plates is shown in Equation (3):

$$\begin{gathered}
P_{ac} = \begin{cases} 0 & \frac{h}{\sigma_p} \geq z \\ \tau E F_{2.5}\left(4 - \frac{h}{\sigma_p}\right) & \frac{h}{\sigma_p} < z \end{cases} \\
\tau = \frac{16\sqrt{2}\pi}{15}(\sigma\beta\delta)2\sqrt{\frac{\delta}{\beta}} \\
E = \frac{1}{\frac{1-v_1^2}{E_1} + \frac{1-v_2^2}{E_1}} \\
F_{2.5}\left(4 - \frac{h}{\sigma_p}\right) = 4.4086 \times 10^{-5}\left(4 - \frac{h}{\sigma_p}\right)^{6.804}
\end{gathered} \quad (3)$$

In the equation, v_1 and v_2 denote the Poisson's ratios of the two materials, respectively; E_1 and E_2 denote the elastic moduli of the two materials, respectively; σ, β, and δ denote the peak roughness, average peak radius, and peak density, respectively, with their values ranging from 0.03 to 0.05 and the value of $\frac{\delta}{\beta}$ ranging from 0.01 to 0.0001; Z is the critical value, which can be taken as 3.5 to 4; h is the clearance; and σ_p is the clearance standard deviation, which is generally taken as 0.1 µm. Then, the normal force on the contact surface between the seal plate and the seal groove can be obtained by integrating the contact pressure, and the rough contact friction coefficient is generally taken as 0.15. According to the above equations, combined with the relevant literature [13,14,43–45], it can be concluded that the equivalent leakage area of radial leakage ranges from 0 mm^2 to 0.5 mm^2. To study the influence of the radial leakage area on in-cylinder flow and combustion, this study calculated the simulation models of the rotary engine with radial equivalent leakage areas of 0 mm^2, 0.08 mm^2, 0.16 mm^2, 0.24 mm^2, 0.32 mm^2, and 0.4 mm^2, respectively.

3.2. The Establishment and Calculation of the 3D Simulation Model for Radial Leakage

Figure 12 shows the rotor radial leakage solid model established based on the rotor solid model built in Section 2, which not only ensures the existence of leakage paths between different cylinders but also ensures that the radial seal between the cylinder block and the rotor is not damaged. As shown in Figure 13, this is the radial leakage simulation model of the rotary engine established based on the aforementioned solid model. To resolve the contradiction between the large-structure solid model and the small-structure leakage gap, this study uses multi-layer refinement and adaptive meshing technology to perform mesh generation on the solid model, and the meshed model is shown in Figure 14.

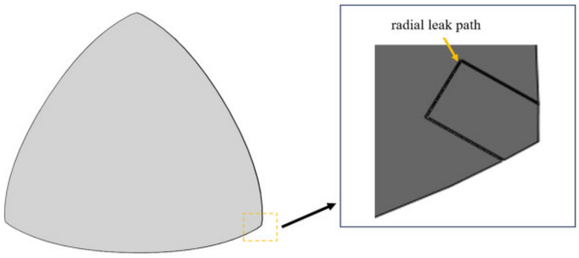

Figure 12. Solid model of radial seal.

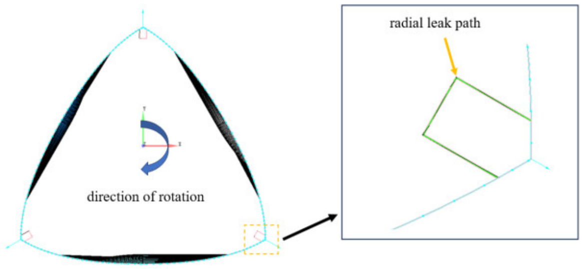

Figure 13. Radial seal simulation model.

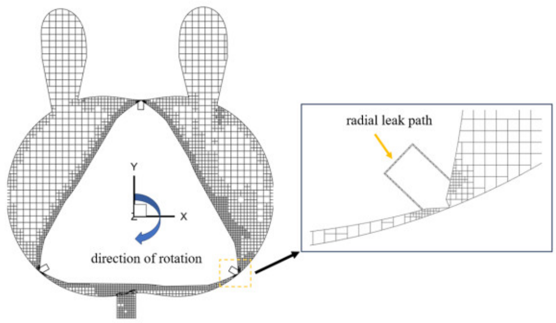

Figure 14. Radial seal mesh model.

Figure 15 shows the contour plots of velocity, pressure, temperature, and turbulent kinetic energy at the leakage location when the equivalent leakage area is 0.16 mm^2. As can be seen from the above figures, there is mass exchange between different cylinders, but the temperature and pressure of different cylinders are different; this indicates that the leakage model not only ensures the existence of mass leakage paths between adjacent cylinders but also ensures that the seal between adjacent cylinders is not completely damaged. Thus, the radial leakage model of the rotary engine established in this section can simulate the radial leakage between different combustion chambers of the rotor.

Figure 16 shows the comparison of peak pressure under different equivalent leakage areas, Figure 17 shows the comparison of minimum in-cylinder mass under different equivalent leakage areas, and Figure 18 also shows the comparison of maximum in-cylinder temperature under different equivalent leakage areas. As can be seen from the figures, as the equivalent leakage area increases, the peak pressure, minimum in-cylinder mass, and maximum in-cylinder temperature all decrease gradually, and the magnitude of the decrease gradually diminishes. This study takes the radial equivalent leakage areas of 0 mm^2, 0.16 mm^2, and 0.4 mm^2 as examples to analyze the influence of different radial equivalent leakage areas on in-cylinder flow and combustion.

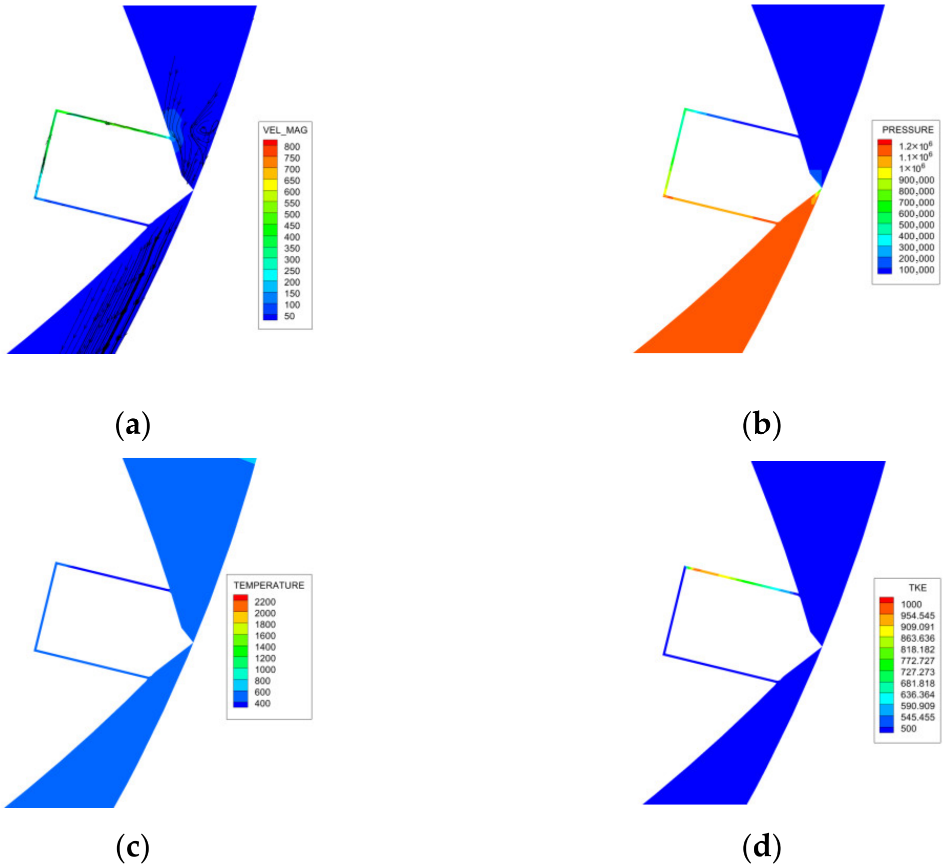

Figure 15. Calculation results at radial leakage. (**a**) Velocity contour, (**b**) pressure contour, (**c**) temperature contour, (**d**) turbulent kinetic energy contour.

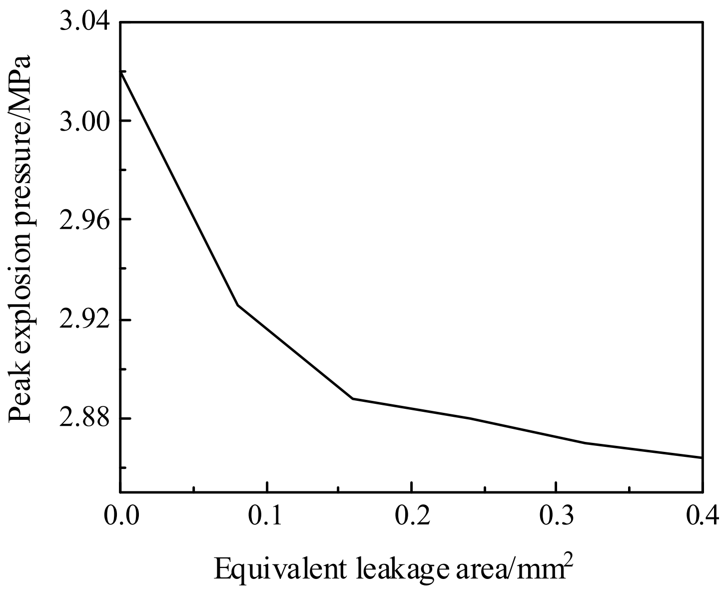

Figure 16. Comparison of peak pressure.

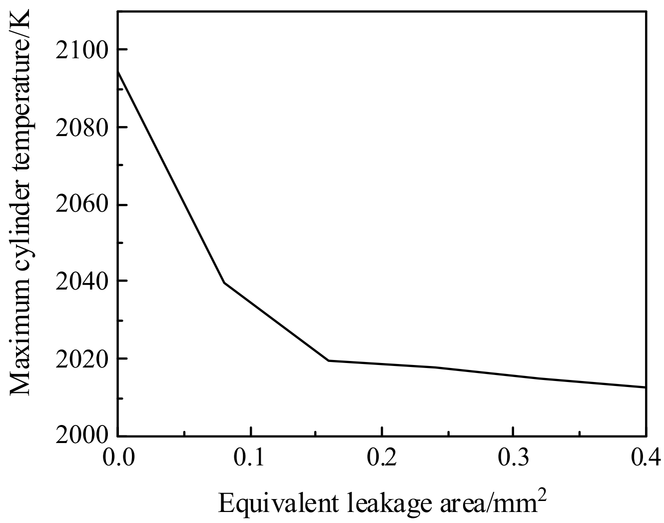

Figure 17. Comparison of maximum in-cylinder temperature.

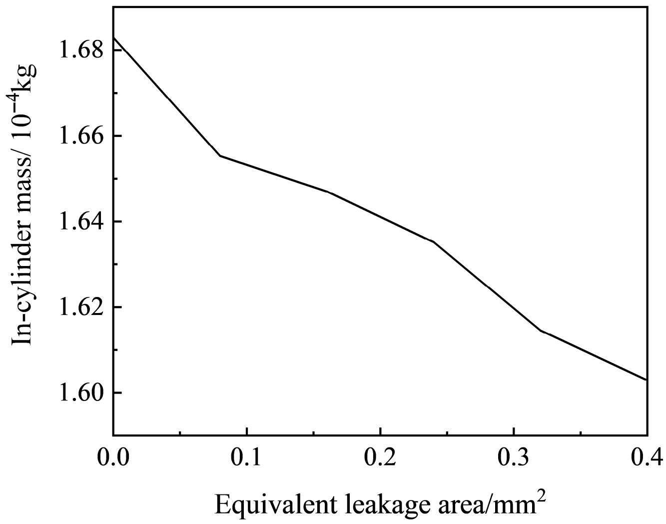

Figure 18. Comparison of minimum in-cylinder mass.

4. Discussion on the Effects of Radial Leakage on In-Cylinder Flow and Combustion Processes

4.1. The Influence of Radial Leakage on In-Cylinder Flow

The operation of a rotary engine is roughly divided into four stages: intake, compression, combustion work, and exhaust, where the intake stage occurs in the time range of −540 °CA to −270 °CA, the compression stage occurs in the time range of −270 °CA to 0 °CA, the combustion stage occurs in the time range of −30 °CA to 270 °CA, and the exhaust stage occurs in the time range of 270 °CA to 540 °CA.

Figure 19 shows the velocity contour plots at Z = 0 m in the XY plane under three equivalent leakage areas at −300 °CA during the intake stage. As can be seen from the figure, during the intake stage, the moving fluid in the cylinder is affected by both the intake port and the rotor motion, resulting in intense disturbance between the fluids in the cylinder and uneven velocity distribution. When there is a leakage issue in the combustion chamber, the influencing factors of fluid motion in the cylinder increase: the fluid is affected by both the forced action of the rotor structure and the leaked gas from adjacent cylinders, inducing the gas in the cylinder to flow out through the leakage holes. During the intake process, the original flow field is affected due to the presence of leakage, leading to more chaotic velocity distribution. Moreover, as the equivalent leakage area increases, the high-velocity fluid regions near the wall surfaces also increase accordingly. The high-velocity fluid distribution regions mainly occur near the front and middle parts of the combustion chamber; as the equivalent leakage area increases, the high-velocity fluid distribution regions expand and the in-cylinder velocity increases. In the no-leakage case and when the equivalent leakage area is 0.16 mm^2, the high-velocity fluid is mainly distributed in the middle of the combustion chamber. When the equivalent leakage area is 0.40 mm^2, the high-velocity fluid spreads from the middle to the front of the combustion chamber, and a large range of low-velocity fluid regions appear near the intake port, which causes a significant deflection in the direction of motion of the fluid entering the cylinder. After a large amount of airflow enters the cylinder, it collides with the rotor wall surfaces near the middle of the combustion chamber, increasing the distribution area of high-velocity fluid in the middle and rear parts of the combustion chamber. When the equivalent leakage area is small, the influence of leakage on the direction of the motion of the fluid entering the cylinder is also small, and so the difference in the distribution area of high-velocity fluid compared with the no-leakage case is minor. However, under the effect of leakage, the amount of fluid that collides with the rotor wall surfaces increases, which is conducive to increasing the flow velocity; therefore, when the equivalent leakage area is 0.16 mm^2, the distribution area of high-velocity fluid in the middle of the combustion chamber is larger than that in the no-leakage case.

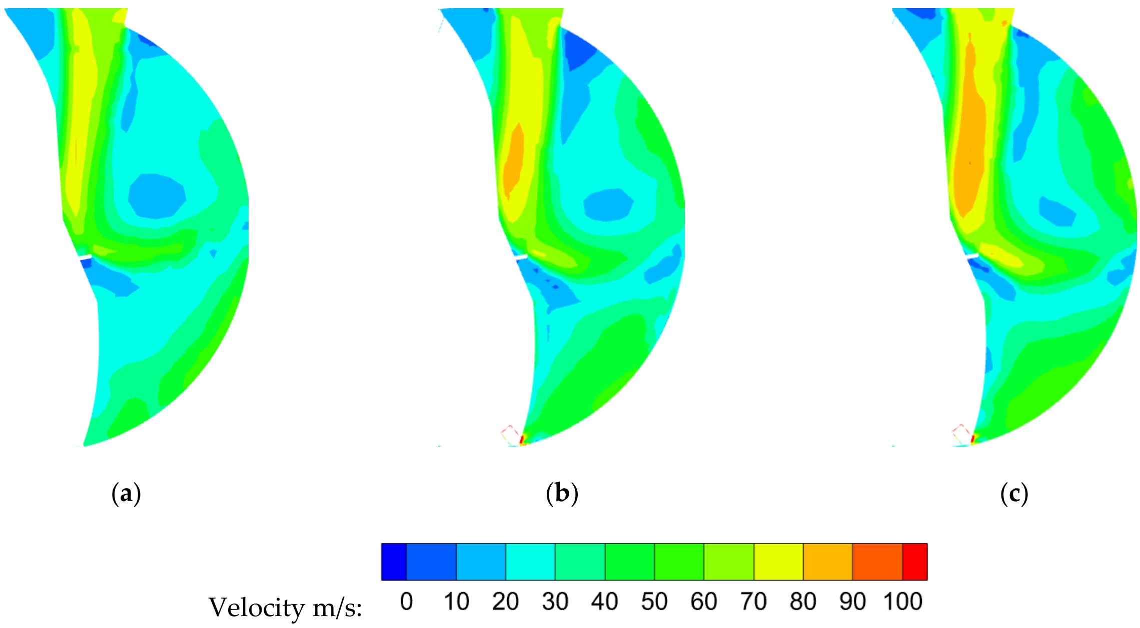

Figure 19. Velocity contour in intake phase. (**a**) Equivalent leakage area 0 mm^2, (**b**) equivalent leakage area 0.16 mm^2, (**c**) equivalent leakage area 0.40 mm^2.

Figure 20 shows the velocity contour plots at Z = 0 m in the XY plane under different equivalent leakage areas at the early (−210 °CA), middle (−120 °CA), and final (−30 °CA) stages of the compression stage. From the figure, it can be seen that, in the early stage of the compression stage, high-velocity fluid is mainly distributed near the rotor and cylinder wall surfaces. As compression proceeds, the in-cylinder flow velocity gradually decreases, while the distribution area of high-velocity fluid near the rotor end face on the spark plug side increases. When the equivalent leakage area is 0.16 mm^2, the in-cylinder velocity distribution is the most orderly; in the no-leakage model and when the equivalent leakage area is 0.40 mm^2, the in-cylinder velocity distribution is relatively chaotic. In the middle stage of compression, the high-velocity fluid concentrated in the spark plug chamber is affected by the leakage paths, leading to an increase in the area of low-velocity fluid regions near the wall surfaces. Moreover, the gas flow in the spark plug chamber exhibits an obvious stratification phenomenon, which becomes more pronounced as the equivalent leakage area of the end face increases—when the equivalent leakage area is 0.40 mm^2, there is almost no high-velocity fluid near the wall surfaces. In the final stage of compression, the flow velocity of the fluid at the far end of the combustion chamber decreases, and the in-cylinder gas flow is mainly laminar flow; however, the area of low-velocity fluid regions hardly changes with the increase in the equivalent leakage area of the end face.

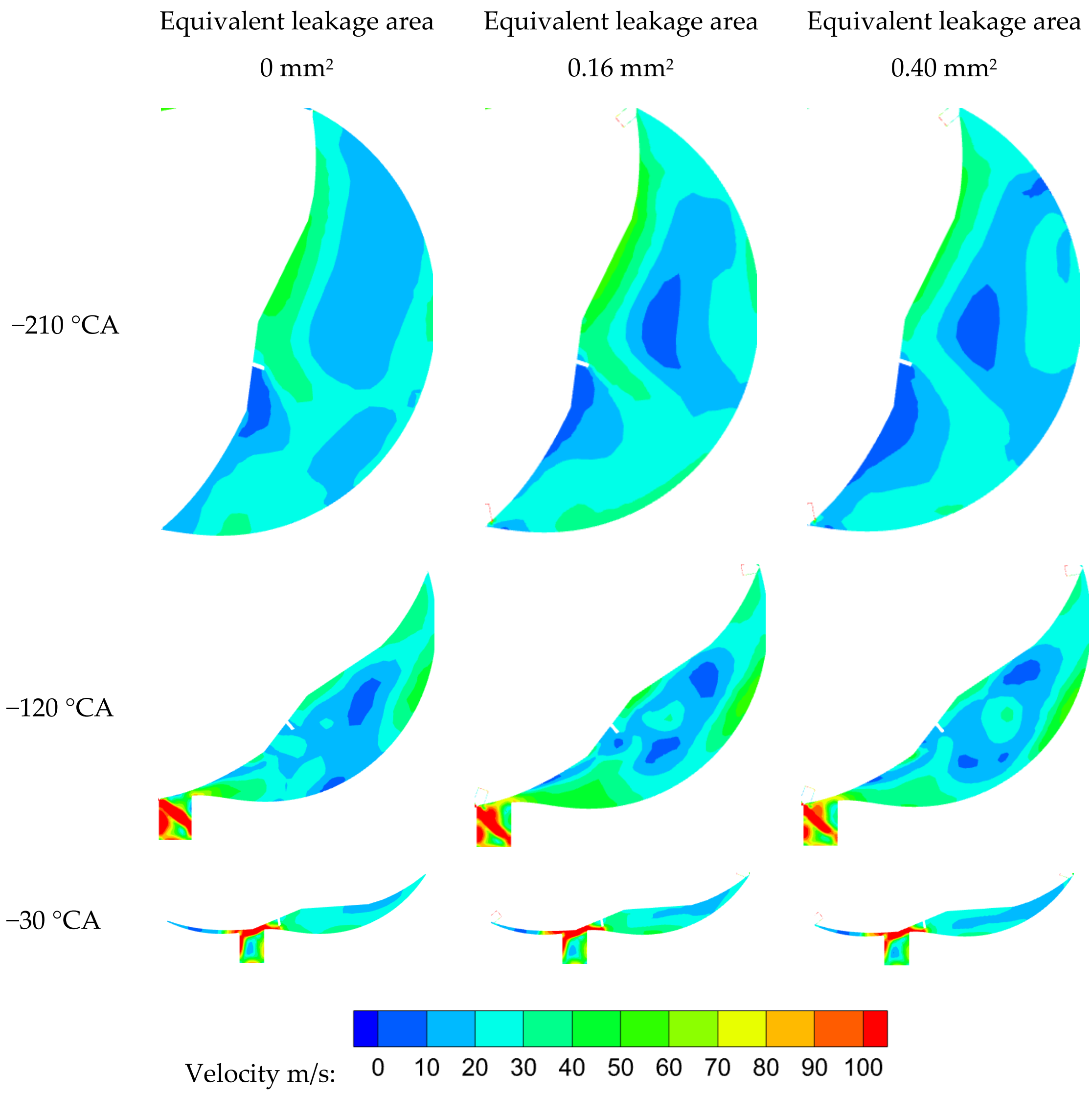

Figure 20. Velocity contour of radial leakage form in compression stage.

Figure 21 shows the velocity contour plots of the models with three equivalent leakage areas at Z = 0 m in the XY plane at the ignition timing. As can be seen from the figure, the presence of radial leakage disrupts the original flow field state, with the most direct manifestation being that the fluid velocity in the front part of the combustion chamber decreases in the middle stage of combustion, and the degree of decrease first increases and then decreases as the equivalent leakage area increases. The fluid velocity in the middle and rear parts of the combustion chamber increases, and the degree of increase rises with the increase in the equivalent leakage area. The greater the difference between the fluid velocity in the middle and rear parts and that in the front part of the combustion chamber, the larger the vortices generated by the strong shear force acting on the low-velocity fluid in the front part and the high-velocity fluid in the middle and rear parts during combustion, which in turn affects flame propagation. The reason for the inconsistent velocity changes at both ends lies in the rotation direction of the rotor—under the influence of rotor rotation, the in-cylinder airflow generally shows a flow trend from the front to the rear part of the combustion chamber along the rotation direction. The presence of leakage turns the original closed-space flow into a semi-open-space flow, resulting in a flow field in the rear part of the combustion chamber that is in the same direction as the overall flow and flows toward the adjacent cylinder, thus increasing the local velocity there, while the flow field in the front part of the combustion chamber is opposite to the overall flow direction. This airflow tearing forms vortices in the middle and rear parts of the combustion chamber, disrupting the flow regularity there, reducing flow energy, and thereby leading to the emergence of a low-velocity region.

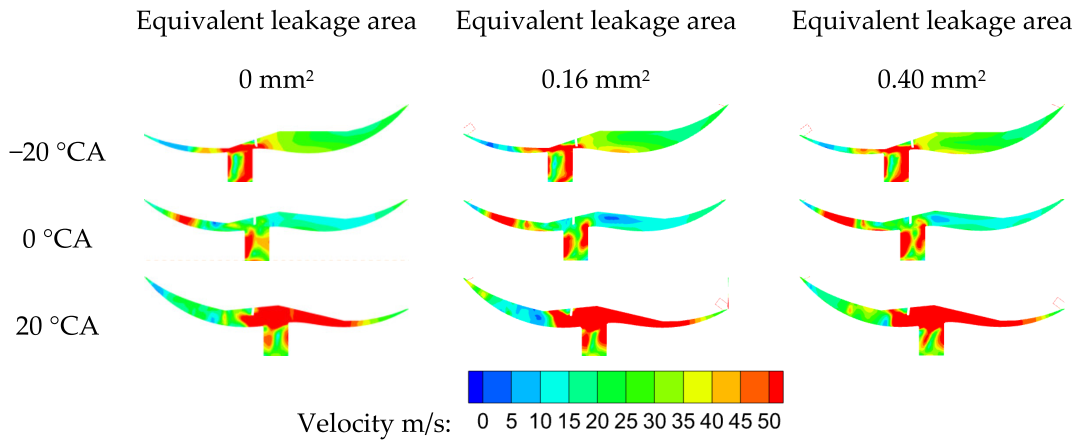

Figure 21. Velocity contours of radial leakage form in the power stage.

4.2. The Influence of Radial Leakage on the Combustion Process

The flame shapes of three models with different equivalent leakage areas at different moments on the XZ plane during the power stroke are shown in Figure 22. Combining this with the analysis of the mechanism of radial leakage on in-cylinder gas flow above, it can be concluded that, affected by the high-velocity fluid in the rear part of the combustion chamber caused by radial leakage, the flame propagation speed along the rotation direction increases slightly and the flame radius enlarges, which promotes flame development and thus helps shorten the ignition delay period. However, compared with the flame shape under the leakage-free state, the presence of radial leakage increases the irregularity of the flame shape, and this is because, in the absence of leakage, flame propagation is mainly affected by the forced gas motion caused by the rotor structure, i.e., under the action of the rotor, and the in-cylinder fluid moves from the front part to the middle and rear parts of the combustion chamber, thereby promoting the flame to propagate toward the middle and rear parts of the combustion chamber. While the presence of radial leakage makes flame propagation affected not only by the rotor, on the one hand, the high-velocity fluid in the rear part of the combustion chamber disperses the force exerted by the rotor on the in-cylinder fluid and flame, changing the fluid flow direction and leading to a trend of the flame tilting toward the combustion chamber wall during propagation, and this trend becomes more obvious as the equivalent leakage area increases. On the other hand, the vortex region in the front part of the combustion chamber reduces the local flow velocity, and the strong shear force generated by its interaction with the high-velocity fluid in the rear part of the combustion chamber intensifies the instability during flame propagation, deteriorates the regularity of flame shape distribution, and results in flame quenching during the middle stage of combustion (10 °CA to 20 °CA).

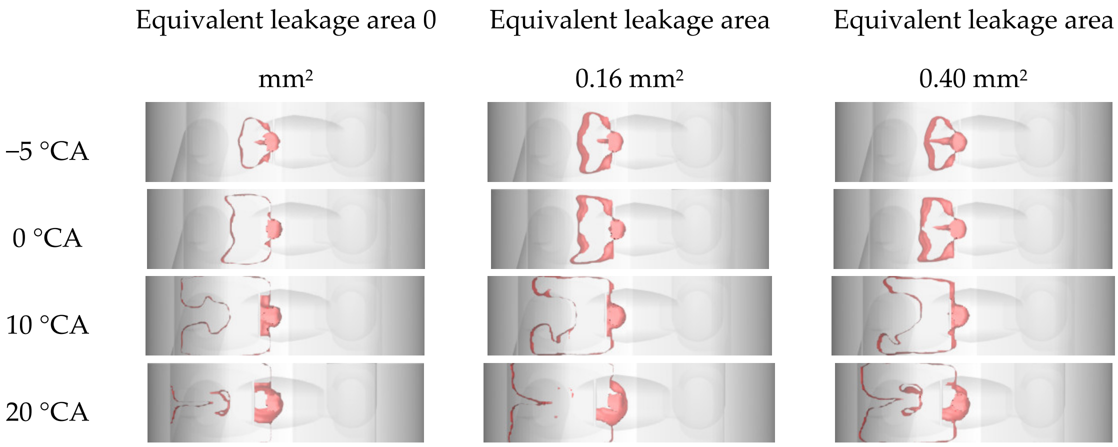

Figure 22. Radial leakage form XZ plane flame shape at work stage.

Figure 23 shows the heat release rate curves of the three models with different equivalent leakage areas. From the figure, it can be seen that the heat release rate of the leakage models starts to rise earlier than that of the no-leakage model. Between −30 °CA and 15 °CA, the heat release rate of the leakage models is consistently higher than that of the no-leakage model, while, after 15 °CA, the rising rate of the heat release rate of the no-leakage model increases and gradually becomes higher than that of the radial leakage models. When radial leakage exists, the combustion start timing is advanced, but the combustion rate is low; furthermore, during the slow combustion period, the rising speed of the heat release rate decreases significantly, and an increase in the equivalent leakage area further reduces the rising rate of the heat release rate. Combined with Figure 22, it can be concluded that the decrease in the rising speed of the heat release rate of the leakage models is caused by irregular flame development. The presence of leakage makes the flame no longer move solely toward the rear of the combustion chamber but instead tilt toward the combustion chamber wall; this leads to an increase in the contact area between the flame and the wall, which in turn results in an increase in flame energy loss. This energy loss makes it difficult to maintain turbulent motion for an extended period. Therefore, the complexity of the in-cylinder flow field shows a significant downward trend and the disturbance of the fluid moving toward the rear of the combustion chamber is weakened, and this further causes a decrease in flame propagation speed and a subsequent decrease in the rising speed of the heat release rate.

Figure 24 shows the in-cylinder pressure, in-cylinder temperature, in-cylinder mass, and leakage mass flow rate for different equivalent leakage areas, where a positive leakage mass flow rate indicates mass flowing from the current combustion chamber to adjacent chambers, and a negative value indicates mass flowing into the current combustion chamber from adjacent ones. From the figure, it can be seen that, when leakage exists, the in-cylinder pressure decreases slightly. In this study, due to the small set of equivalent leakage areas, the variation trends of in-cylinder pressure and temperature are almost consistent across different equivalent leakage areas, and the peak in-cylinder pressure and peak in-cylinder temperature are nearly the same. The presence of radial leakage reduces the distribution area of high-velocity fluid along the rotor direction, which affects flame propagation. A large-area flame quenching phenomenon occurs during the combustion process, which reduces combustion efficiency, thereby causing a more significant decrease in in-cylinder pressure and temperature and lowering engine performance. The leakage mass flow rate increases with the increase in equivalent leakage area and reaches its maximum value around 180 °CA.

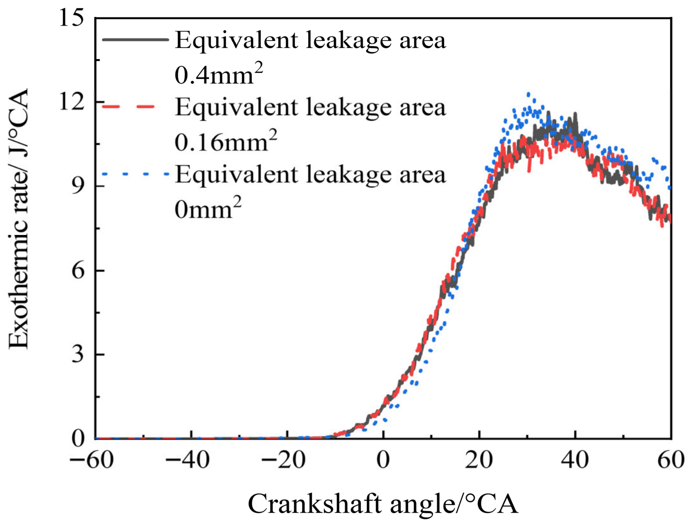

Figure 23. Radial leakage heat release rate.

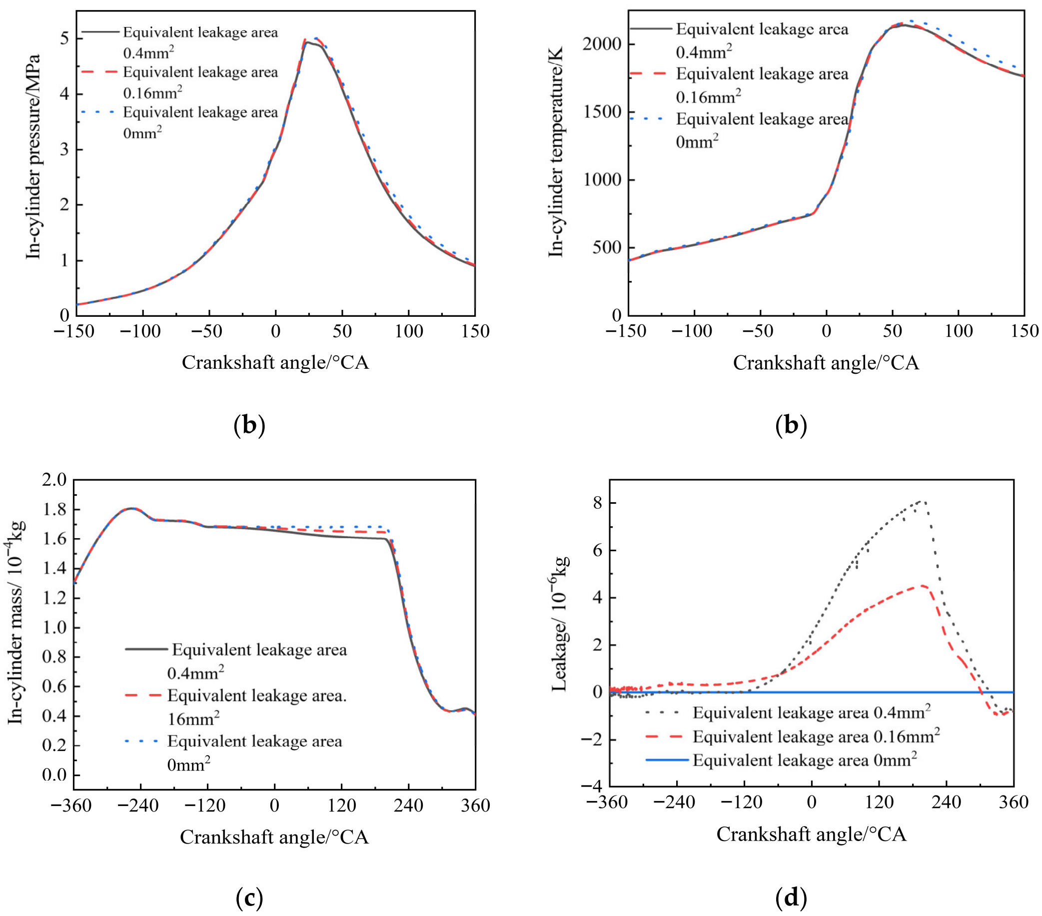

Figure 24. Performance comparison. (**a**) Radial leakage cylinder pressure, (**b**) radial leakage cylinder temperature, (**c**) radial leakage cylinder mass, (**d**) leakage mass of radial leakage.

5. Conclusions

To investigate the leakage characteristics of radial leakage and equivalent leakage area, this study, by referring to relevant domestic and international literature, defines the leakage mode of the rotary engine—occurring at the gaps between radial seal plates, seal plate grooves, and the cylinder block—as radial leakage. Based on this definition, the study establishes a leakage model for the rotary engine considering radial leakage and investigates the influence of the laws and action mechanisms of radial leakage and equivalent leakage area on in-cylinder gas flow, combustion process, and engine performance. The main conclusions of this study are as follows:

1. Compared with the leakage-free model, the presence of radial leakage can change the in-cylinder gas flow state, slightly increase the flame radius, improve the flame propagation speed, and, especially, accelerate the flame propagation along the combustion chamber wall, thereby promoting the overall flame development and further shortening the combustion ignition delay period. However, the presence of leakage, on the one hand, disperses the force exerted by the rotor on the in-cylinder fluid and flame, changing the fluid flow direction and leading to a tendency of the flame tilting toward the rotor wall during propagation, and, on the other hand, it also increases the distribution area of high-velocity fluid in the middle and rear parts of the combustion chamber, reduces the overall flow velocity in the front part of the combustion chamber, and enhances the vortex intensity generated by the strong shear force acting on the low-velocity fluid in the front part and the high-velocity fluid in the middle and rear parts of the combustion chamber during the combustion process, which further intensifies the instability of the flame during propagation, deteriorates the regularity of flame shape distribution, and eventually leads to a large-area flame quenching phenomenon, thereby reducing the combustion efficiency and resulting in a relatively significant decrease in both in-cylinder pressure and temperature.
2. An increase in the equivalent leakage area further intensifies the negative effects caused by radial leakage. Radial leakage leads to an earlier start of combustion but a slower combustion rate, with the increased rate of heat release rate during the slow combustion period decreasing significantly, and, the larger the equivalent leakage area, the more significant the reduction in the increase rate of the heat release rate. When leakage exists, both in-cylinder pressure and temperature decrease significantly, with almost consistent variation trends and almost the same peak values. The leakage rate caused by radial leakage increases with the increase in the equivalent leakage area and reaches a maximum around 180 °CA, and the change in leakage rate further exacerbates the instability of in-cylinder mass distribution, which, combined with the decrease in combustion efficiency, exerts an adverse impact on the overall performance of the engine.

Author Contributions: Methodology, Y.L.; Validation, S.Y.; Investigation, Y.Z.; Resources, L.L., Y.L. and R.Z.; Data curation, L.L. and S.Y.; Writing—review & editing, Y.Z.; Visualization, Y.Z.; Supervision, Y.L.; Project administration, L.L., S.Y. and R.Z.; Funding acquisition, Y.Z. and R.Z. All authors have read and agreed to the published version of the manuscript.

Funding: This work was supported by the Applied Basic Research Programs of Shanxi Province in China (Grant No. 202203021222045).

Institutional Review Board Statement: Not applicable.

Informed Consent Statement: Not applicable.

Data Availability Statement: The original contributions presented in this study are included in the article. Further inquiries can be directed to the corresponding author.

Conflicts of Interest: The authors declare no conflict of interest.

References

1. Meng, H.; Ji, C.; Wang, S.; Yang, J. A review: Centurial progress and development of Wankel rotary engine. *Fuel* **2023**, *335*, 127043. [CrossRef]
2. Shimizu, R.; Tadokoro, T.; Nakanishi, T.; Funamoto, J. Mazda 4-rotor rotary engine for the Le Mans 24-hour endurance race. In *Prototype Powertrain in Motorsport Endurance Racing: An SAE Technical Paper Compilation*; SAE International: Warrendale, PA, USA, 2018; p. 51.
3. Su, T.; Ji, C.; Wang, S.; Cong, X.; Shi, L. Research on performance of a hydrogen/n-butanol rotary engine at idling and varied excess air ratios. *Energy Convers. Manag.* **2018**, *162*, 132–138. [CrossRef]
4. Meng, H.; Ji, C.; Su, T.; Yang, J.; Chang, K.; Xin, G.; Wang, S. Analyzing characteristics of knock in a hydrogen-fueled Wankel rotary engine. *Energy* **2022**, *250*, 123828. [CrossRef]
5. Zhang, Y.; He, W.; Hu, L.; Lou, Z.; Zhang, D.; Wang, Z. Prediction of rotary seal leakage rate under the influence of stress relaxation based on G A-PSO-BP hybrid algorithm. *Eng. Res. Express* **2025**, *7*, 015581. [CrossRef]
6. Chen, Y.; Cai, C.; Liu, G. Experimental analysis of clearance leakage characteristics at blade edge plates of a gas turbine engine. *Energies* **2022**, *15*, 2303. [CrossRef]
7. Kim, M.J.; Kim, J.H.; Kim, T.S. The effects of internal leakage on the performance of a micro gas turbine. *Appl. Energy* **2018**, *212*, 175–184. [CrossRef]
8. Ai, Y.; Han, S.; Tian, J.; Liu, Y.; Yao, Y.; Guan, J.; Zhang, Y. Experimental study and comprehensive analysis of leakage characteristics of the casing flange of an aero-engine. *Therm. Sci. Eng. Prog.* **2024**, *47*, 102321. [CrossRef]
9. Turnbull, R.; Dolatabadi, N.; Rahmani, R.; Rahnejat, H. An assessment of gas power leakage and frictional losses from the top compression ring of internal combustion engines. *Tribol. Int.* **2020**, *142*, 105991. [CrossRef]
10. Jiaqiang, E.; Liu, G.; Zhang, Z.; Han, D.; Chen, J.; Wei, K.; Gong, J.; Yin, Z. Effect analysis on cold starting performance enhancement of a diesel engine fueled with biodiesel fuel based on an improved thermodynamic model. *Appl. Energy* **2019**, *243*, 321–335. [CrossRef]
11. Hu, J.; Yu, Y.; Yang, J.; Jia, H. Research on the generalisation method of diesel engine exhaust valve leakage fault diagnosis based on acoustic emission. *Measurement* **2023**, *210*, 112560. [CrossRef]
12. Fan, B.; Zhang, Y.; Pan, J.; Otchere, P.; Wang, Y.; Zeng, Y. The formation mechanisms of flow field in a compound intake ported rotary engine considering apex seal leakage. *Environ. Prog. Sustain. Energy* **2020**, *39*, e13432. [CrossRef]
13. Yang, Z.; Ji, C.; Huang, X.; Yang, J.; Wang, H.; Wang, S. Modeling and analysis of apex seal leakage in a hydrogen fueled Wankel rotary engine. *Fuel* **2023**, *331*, 125848. [CrossRef]
14. Fan, B.; Wang, Y.; Zhang, Y.; Pan, J.; Yang, W.; Zeng, Y. Numerical Investigation on the Combustion Performance of a Natural Gas/Hydrogen Dual Fuel Rotary Engine under the Action of Apex Seal Leakage. *Energy Fuels* **2021**, *35*, 770–784. [CrossRef]
15. Picard, M.; Tian, T.; Nishino, T. Predicting Gas Leakage in the Rotary Engine—Part I: Apex and Corner Seals. *J. Eng. Gas Turbines Power* **2015**, *138*, 062503. [CrossRef]
16. Zhou, X.; Zhang, Z.; Kong, W.; Du, N. Investigations of leakage mechanisms and its influences on a micro swing engine considering rarefaction effects. *Appl. Therm. Eng.* **2016**, *106*, 674–680. [CrossRef]
17. Fan, B.; Wang, Y.; Pan, J.; Zhang, Y.; Zeng, Y. Numerical study on flow field in a peripheral ported rotary engine under the action of apex seal leakage. *J. Fluids Eng.* **2021**, *143*, 041205. [CrossRef]
18. Ji, C.; Yang, Z.; Yang, J.; Wang, S. Apex seal bottom pressure prediction and leakage analysis of The Hydrogen Fueled Wankel Rotary Engine based on dynamics. *Int. J. Hydrogen Energy* **2022**, *47*, 22226–22242. [CrossRef]
19. Fan, B.; Zeng, Y.; Zhang, Y.; Pan, J.; Yang, W.; Wang, Y. Research on the hydrogen injection strategy of a direct injection natural gas/hydrogen rotary engine considering apex seal leakage. *Int. J. Hydrogen Energy* **2021**, *46*, 9234–9251. [CrossRef]
20. Fan, B.; Zeng, Y.; Pan, J.; Fang, J.; Salami, H.A.; Wang, Y. Evaluation and analysis of injection strategy in a peripheral ported rotary engine fueled with natural gas/hydrogen blends under the action of apex seal leakage. *Fuel* **2022**, *310*, 122315. [CrossRef]
21. Shi, C.; Ji, C.; Ge, Y.; Wang, S.; Yang, J.; Wang, H. Effects of split direct-injected hydrogen strategies on combustion and emissions performance of a small-scale rotary engine. *Energy* **2021**, *215*, 119124. [CrossRef]
22. Ji, C.; Li, H.; Yang, J.; Meng, H. Numerical investigation on the effect of ignition timing on a low-temperature hydrogen-fueled Wankel rotary engine with passive pre-chamber ignition. *Energy* **2024**, *313*, 133686. [CrossRef]
23. Yang, Z.; Ji, C.; Yang, J.; Wang, H.; Huang, X.; Wang, S. The optimization of leading spark plug location and its influences on combustion and leakage in a hydrogen-fueled Wankel rotary engine. *Int. J. Hydrogen Energy* **2023**, *48*, 20465–20482. [CrossRef]
24. Yang, J.; Zhang, Y.; Cong, X.; Sun, Y.; Li, H.; Yang, Z.; Ji, C. The effect of leakage characteristics of spark plug cavity on flow and combustion performances in a hydrogen Wankel rotary engine. *Int. J. Hydrogen Energy* **2025**, *109*, 1114–1125. [CrossRef]
25. Kurien, C.; Rousselle, C. Comparative Study On The Effect Of Premixed Equivalence Ratio On Engine Characteristics of Ammonia Fuelled Engine Under Diesel Pilot Ignition vs Spark Igition Combustion Mode. *J. Eng. Gas Turbines Power* **2025**, *147*, 101005. [CrossRef]

26. Mahmoud, H.; Vlasic, F.; Mazal, P.; Jana, M. Leakage analysis of pneumatic cylinders using acoustic emission. *Insight Non-Destr. Test. Cond. Monit.* **2017**, *59*, 500–505. [CrossRef]
27. Kumar, A.; Chaudhari, A.; Patel, V.B. Optimizing tooth count in labyrinth seals for enhanced efficiency and reduced leakage in centrifugal compressors: A computational fluid dynamics study. *Sādhanā* **2025**, *50*, 166. [CrossRef]
28. Jun, G.; Yayun, H. Analysis and detection method of cylinder leakage. *Automob. Manuf. Ind.* **2019**, *44–45*, 52.
29. Deng, C.; Song, P. Grid independence analysis in the numerical simulation of spiral groove dry gas seals. *Lubr. Eng.* **2016**, *41*, 86–90+101.
30. Yu, T.; Lee, D.E.; Alam, A.; Gore, J.P.; Qiao, L. Exploring H_2/O_2 Injection in an Active Pre-Chamber Ignition Engine. *SAE Int. J. Engines* **2025**, *18*, 229–248. [CrossRef]
31. Wang, Y.; Hu, Q.; Sun, J.; Wang, D.; Zheng, X. Numerical analysis of T-groove dry gas seal with orientation texture at the groove bottom. *Adv. Mech. Eng.* **2019**, *11*, 1–12. [CrossRef]
32. Xu, Y. Research on Combustion Characteristics and Range-Extending Power Generation of Multi-Fuel Rotary Engine. Ph.D. Thesis, Xiangtan University, Xiangtan City, China, 2024. [CrossRef]
33. Kuang, X.; Yang, X.; Li, S.; Sun, X.; Li, C. Design and calibration of an electronic ignition system for general-purpose small gasoline engines. *Small Intern. Combust. Engine Veh. Tech.* **2025**, *54*, 35–39.
34. Li, H.; Sun, F. Application Development and Key Technologies of Rotary Engine. *Small Intern. Combust. Engine Veh. Tech.* **2023**, *52*, 68–74.
35. Li, H. A 45cc Diesel Rotary Engine. Jiangxi Zhuochao Technology Co., Ltd., Jiangxi Province, China. 12 January 2024. Available online: https://kns.cnki.net/kcms2/article/abstract?v=4qE7rfs4XRFaTcb6JQMITMA1MgCnEtwFQQjV9BrcKmx4K6-frJABJ74ToLl2xyXTGCL2-amE-VOhvxlY73FZRL7d0ghd7zrN3iWpCIB4JZX67bBK9E2pvHTCSn555AJCe6Y1lPWWi5QybvZs63115Pd7m_ATywNa6EDAQ0XXhO0=&uniplatform=NZKPT&language=CHS (accessed on 5 October 2025).
36. Qin, C. A Rotary Engine Seal. Chinese Patent Application No. CN201911107644. X, 31 October 2025.
37. Picard, M.; Tian, T.; Nishino, T. Predicting Gas Leakage in the Rotary Engine—Part II: Side Seals and Summary. *J. Eng. Gas Turbines Power* **2016**, *138*, 062504. [CrossRef]
38. Wang, K.; Li, X.; Du, B. Grid independence analysis in the numerical simulation of T-groovedry gas seals. *Digit. Des.* **2017**, *6*, 66–69.
39. Lei, J.; Liu, C.; Deng, X.; Deng, W.; Jia, D.; Liu, Q. Radial Seal Structure of a Rotary Engine. Chinese Patent Application No. CN202310823932.5, 1 November 2025.
40. Chen, T.; Lei, J.; Deng, X.; Zhang, Y.; Wang, R.; Li, H. Influence of injection strategy on the combustion process of diesel rotary engine under radial seal leakage. *Intern. Combust. Engine Eng.* **2023**, *44*, 34–43.
41. Wei, Z.; Tao, Y.; Fengtao, G.; Yang, W.; Xinghai, W. Effect of cylinder block offset on radial seal movement of rotor engine. *Intern. Combust. Engine Accessories* **2022**, *10*, 47–49. [CrossRef]
42. Ji, C.W.; Yang, Z.Y.; Yang, J.X.; Wang, S.F.; Huang, X.H.; Chang, K. Research overview of rotary engine apex seals. *Chin. J. Eng.* **2022**, *44*, 1406–1424.
43. Warren, S.R.; Ch, D.Y. Wide and multiple apex seals for the rotary engine. *Mech. Mach. Theory* **2013**, *74*, 202–215.
44. Li, L.; Tang, D.; Fang, J.; Wang, X. Simulation of a Dynamic Behavior of Apex Seals in Rotary Engine. *Lubr. Eng.* **2003**, *2*, 3–5. Available online: https://kns.cnki.net/kcms2/article/abstract?v=4qE7rfs4XRGa_li4rtNbz4-ufp4kztu6aJHpOtcDDt4nH_YmIHNrh1Iftr_HgA5fOUGfwrdJtfdEOPuoclX1kDjh1IKNprYCOpcU9qZ3w8Q8A40ge1faePexN5A2DB9HQHI0BGEswBZAC-wpApC-Tus1XmCiAYHXgmEoRf9Ll8MUF5OfJxizXA==&uniplatform=NZKPT&language=CHS (accessed on 5 October 2025).
45. Eberle, M.K.; Klomp, E.D. An evaluation of the potential performance gain from leakage reduction in rotary engines. *SAE Trans.* **1973**, *82*, 454–460.